*Solar-Terrestrial Physics. 2026, vol. 12, iss.3, pp. 95–101. DOI: 10.12737/stp-123202611. © 2026 S.V. Titov, S.V. Nikolashkin, N.E. Sidorov. Published by INFRA-M Academic Publishing House*

DOI: 10.12737/stp-123202611
EDN: JRSVAH

Received October 21, 2025
Accepted March 02, 2026

# THE POTENTIAL ENERGY DENSITY OF GRAVITY WAVES IN THE WINTER STRATOSPHERE AND LOWER MESOSPHERE FROM LIDAR MEASUREMENTS OVER YAKUTSK

**S.V. Titov**
*Yu.G. Shafer Institute of Cosmophysical Research and Aeronomy SB RAS,*
*Yakutsk, Russia, stitov@ikfia.ysn.ru*

**S.V. Nikolashkin**
*Yu.G. Shafer Institute of Cosmophysical Research and Aeronomy SB RAS,*
*Yakutsk, Russia, nikolashkin@ikfia.ysn.ru*

**N.E. Sidorov**
*Yu.G. Shafer Institute of Cosmophysical Research and Aeronomy SB RAS,*
*Yakutsk, Russia, SidorovNikolay@ikfia.ysn.ru*

**Abstract.** This paper analyzes the characteristics of atmospheric gravity wave activity in the stratosphere and lower mesosphere during the winters from 2010 to 2017 by calculating their potential energy per unit mass from variations in the temperature profile obtained from lidar measurements near Yakutsk, Russia (62° N, 129° E). The most common vertical wavelengths identified through wavelet analysis are 4–6 km and 8–12 km. We examine temporal and altitude variability of waves with vertical wavelengths from 2 km to 20 km and a temporal resolution 10–20 min. The minimum and maximum values of the gravity wave potential energy density (GWPED) per unit mass vary from 5–10 J/kg at an altitude of 30 km to 100–250 J/kg at an altitude of 60 km. Moreover, the most significant variations in the potential energy of gravity waves are observed during sudden winter stratospheric warmings.

**Keywords:** lidar, internal gravity waves, wavelet analysis, Brunt — Väisälä frequency, IGW potential energy density (GWPED).

## INTRODUCTION

Internal gravity waves (IGWs) in the atmosphere play a crucial role in transferring momentum and energy from the lower atmosphere to the upper atmosphere, although, as recent studies have noted, the transfer can also take place from the upper atmosphere to the underlying layers [Strelnikova et al., 2020]. Thus, IGWs have a significant effect on the dynamic processes in Earth's atmosphere. There are many IGW sources: cyclones, atmospheric convection, wind shears, jet streams, orographic features of the terrain, and interactions between different waves in the atmosphere. In the middle atmosphere, the horizontal wavelength of IGW is from tens to several thousand kilometers; and the vertical wavelength, from a few to tens of kilometers [Holton, 1982; Fritts, Alexander, 2003].

To date, insufficient experimental studies have been conducted to fully understand how IGWs affect thermodynamic characteristics of the atmosphere. The purpose of such studies is to improve IGW parameterization in corresponding models [Cai et al., 2017], especially in the height ranges in which a critical layer is formed, where IGWs interact with mean zonal winds, their energy is dissipated, and momentum is transferred [Lindzen, 1981; Matsuno, 1982]. The critical layer is a region in a stratified medium, where the horizontal phase velocity of the wave coincides with the velocity of the background flux. In the mesosphere, this region is at altitudes of ~80–85 km, where atmospheric waves (gravity and tidal) propagating from below are destroyed and dissipated. Thus, the mesosphere is the most active zone of formation of a critical layer, where most IGWs are absorbed, which slows down the zonal wind and drives the global circulation from the summer pole to the winter one. In the stratosphere, a critical layer is usually formed at altitudes higher than 35 km in the region of jet streams and strong vertical wind shears, particularly during sudden stratospheric warming (SSW) events. From this point of view, the high-latitude stratosphere and mesosphere are of great interest to researchers.

Lidar scattering is one of the effective methods for probing IGW activity in the atmosphere from the troposphere to the thermosphere [Wilson et al., 1991; Whiteway, Carswell, 1995; Alpers et al., 2004; Sivakumar et al., 2006; Kafle, 2009; Thurairajah et al., 2010; Mzé et al., 2014; Khaykin et al., 2015; Kaifler et al., 2017, 2020; Dornbrack et al., 2017; Chu et al., 2018; Gisinger et al., 2022]. The atmospheric lidar (Light Detection and Ranging) is an instrument that uses laser pulses to study the atmosphere (aerosols, clouds, temperature, and wind). The lidar is similar to radar in design. Lidars differ in the principle of operation of a receiver, which is based on a specific physical process (phenomenon). For instance, to determine the atmospheric temperature from the Earth surface to an altitude of ~30 km, Raman scattering is measured to exclude the influence of atmospheric aerosols of various origins (the so-called Raman channel). At altitudes from approximately 25 to 90 km, elastic scattering of light by air molecules is estimated; the lower boundary is defined by the aerosol content (Rayleigh channel). Above 80 km, resonant scattering by metal atoms of meteoric origin excited by laser light is used; the lower and upper boundaries depend on the thickness of the layer of the substance in question (resonance channel). Observations with such lidar systems are limited only by weather conditions above the observation point (cloudless atmosphere). Most IGW studies using lidars over the past three decades have been based on Rayleigh lidar measurements due to the well-developed experimental methods, the theoretical basis for subsequent calculation of atmospheric parameters, and the relatively low-cost instrumentation of such devices. Advantages of the lidar method include the possibility of conducting long-term observations with high vertical and time resolution.

At present, many ground-based and satellite instruments have appeared which enable us to examine IGW parameters in Earth's atmosphere. While each instrument performs measurements in its own spectral range, there are overlap zones, where it is possible to compare and validate the IGW parameters obtained by different instruments. A commonly accepted characteristic of IGW employed to interpret ground and satellite data is the so-called gravity wave potential energy density (GWPED) (per unit mass and density) [Hei et al., 2008; Khaykin et al., 2015], which is calculated from variations in the temperature profile or density of Earth's atmosphere. This paper analyzes the IGW activity by estimating their potential energy density per unit mass [Sivakumar et al., 2006; Mzé et al., 2014; Zhao et al., 2022a, b] from data obtained near Yakutsk (62° N, 129°E) for 362 nights of lidar observations from October 2010 to March 2017 in the altitude range from 30 to 60 km.

## 1. DATA AND METHODS

### 1.1. Rayleigh lidar and data

We have used data from the Rayleigh lidar, which from 2004 to 2017 was located 55 km south of Yakutsk, and since 2018 it has been functioning as a mobile version at the Maimaga optical station (63° N, 129° E), located 115 km north of Yakutsk [Titov, Nikolashkin, 2020]. The observations were carried out at night in clear weather with a vertical resolution of 50 m and a time resolution of 10–20 min. The main characteristics of the lidar are given in Table 1.

We employ data collected from 2010 to 2017 during winter periods (from December to February). We ignore data with a continuous observation time of less than two hours and a gap of more than 7 days in order to adequately present monthly average data. In total, 144 days (161 hrs) of data with daily observation time of 2 to 5 hrs have been processed. Temperature profiles are available up to 55–65 km depending on the noise level. Typical measurement errors increase from ~0.2 to 6 K in the probing range from 20 to 60 km respectively. We do not use temperature data below 20–30 km due to the sporadic presence of stratospheric aerosols at these altitudes, which give rise to significant uncertainties when constructing the temperature profile. Time distribution of the temperature measurements is shown in Table 2.

Table 1

Main characteristics of the lidar

| | |
|---|---|
| Laser type | Nd:YAG |
| Pulse repetition rate, Hz | 20 |
| Wavelength, nm | 532 |
| Output pulse energy, mJ | 195 |
| Telescope | Newton system |
| Mirror diameter, m | 0.6 |
| Focal length, m | 2 |
| Field of view, mrad | 0.2 |
| Type of photomultiplier | Hamamatsu H8259-01 |
| Maximum sounding height, km | to 65 |
| Vertical resolution, m | from 50 and higher |

Table 2

Duration of sounding in winter months from 2010 to 2017

| | December, days (hours) | January, days (hours) | February, days (hours) | In total, days (hours) |
|---|---|---|---|---|
| 2010–2011 | 16 d (25 hr 5 min) | 6 d (10 hr 50 min) | 6 d (9 hr 10 min) | 28 d (35 hr 5 min) |
| 2011–2012 | 8 d (10 hr 20 min) | 10 d (13 hr 40 min) | 8 d (10 hr 40 min) | 26 d (34 hr 40 min) |
| 2012–2013 | 7 d (10 hr) | 10 d (10 hr 30 min) | 6 d (4 hr 25 min) | 23 d (24 hr 5 min) |
| 2013–2014 | 1 d (35 min) | 9 d (6 hr 40 min) | 2 d (50 min) | 12 d (2 hr 5 min) |
| 2014–2015 | 3 d (1 hr 15 min) | 2 d (1 hr 15 min) | 5 d (2 hr 25 min) | 10 d (4 hr 55 min) |
| 2015–2016 | 2 d (1 hr 45 min) | 6 d (3 hr 20 min) | 8 d (5 hr 5 min) | 16 d (10 hr 10 min) |
| 2016–2017 | – | 6 d (10 hr 50 min) | 5 d (5 hr 15 min) | 11 d (16 hr 5 min) |

### 1.2. Method of calculating variations in the atmospheric temperature profile

To determine the temperature profile from lidar measurements, we adopt the method [Chanin, Hauchecorne, 1981] based on elastic scattering of laser light by air molecules (Rayleigh scattering), ideal gas laws, and hydrostatic conditions. It is known that atmospheric temperature profile variations are caused by wave disturbances of different spatial and temporal scales. When analyzing IGW, it is generally assumed that

$$T(h,t) = T'(h,t) + T_o(h,t), \quad (1)$$

where $T'(h, t)$ and $T_o(h, t)$ are variational and background components of $T(h, t)$ respectively. To find IGW-driven temperature variations from lidar data, we should exclude the background atmospheric temperature $T_o(h,t)$. $T(h,t)$ consists of a background temperature profile and a superposition of all atmospheric waves, such as planetary, tidal, and internal gravity. It is difficult to estimate $T_o(h,t)$ because of the specific shape of the temperature profile with changes in the vertical gradient, for example, in the stratopause or mesopause regions. The simplest method of gauging $T_o(h,t)$, which is widely applied to lidar measurements, is to use the time profile of the average temperature. For example, Chu et al. [2018] have employed a sixth-order Butterworth high-pass filter to remove waves with periods of more than 11 hrs and vertical lengths of >30 km. Other studies adopted the sliding polynomial fitting procedure [Alexander et al., 2008; Kaifler et al., 2017]. Ehard et al. [2014] have evaluated the most common filtering methods applied to lidar observations, using synthetic data. They concluded that the Butterworth filter is best suited for calculating the background temperature profile over a wide range of periods. The moving average method described in [Ehard et al., 2014] gave reliable results when analyzing short-period IGWs.

In this paper, the temperature profiles with >15 K uncertainty are omitted from consideration in order to ensure higher reliability of the data. Most measurement errors are caused by changes in atmospheric transparency along the sounding path due to clouds, fog, haze, smoke from building heating systems, etc. Background temperature profiles for each profile are computed by the moving average method with a window of 2 km for high-frequency filtering and a fourth-order polynomial for low-frequency one.

### 1.3. Method of determining IGW characteristics

Wavelet analysis is an indispensable mathematical tool for studying nonstationary signals. Unlike Fourier analysis, which decomposes the signal into the sum of the sine and cosine functions, the wavelet analysis decomposes the signal into a finite number of localized wavelets, i.e. it localizes signatures both in time and frequency. The continuous wavelet transform (CWT) provides a continuous representation of a signal in the time — frequency (or distance — wavenumber) domain, which makes it useful for analyzing signals that exhibit time-dependent frequency changes. An example of such nonstationary signals is air temperature disturbances triggered by atmospheric IGWs (Figure 1).

The wavelet transform is often applied to lidar measurements of the atmospheric temperature profile (e.g., [Torrence, Compo, 1998; Kaifler et al., 2017]). In this paper, we use the CWT to find dominant vertical lengths of IGW. As in [Reichert et al. 2024], we employ the fourth-order Morlet wavelet. Profiles of atmospheric temperature variations with a vertical resolution of 50 m and a time resolution of 10 and 20 min showed the presence of vertical quasi-monochromatic wavelike structures (QMWS) throughout the sounding altitude range almost every night. The wavelet analysis identified the most common QMWS whose vertical lengths were 4–6 and 8–12 km (Figure 2). Note that short-wave quasi-monochromatic structures predominate during winter SSW events, which is in good agreement with theoretical and experimental works [Fritts, Alexander, 2003; Rauthe et al., 2006].

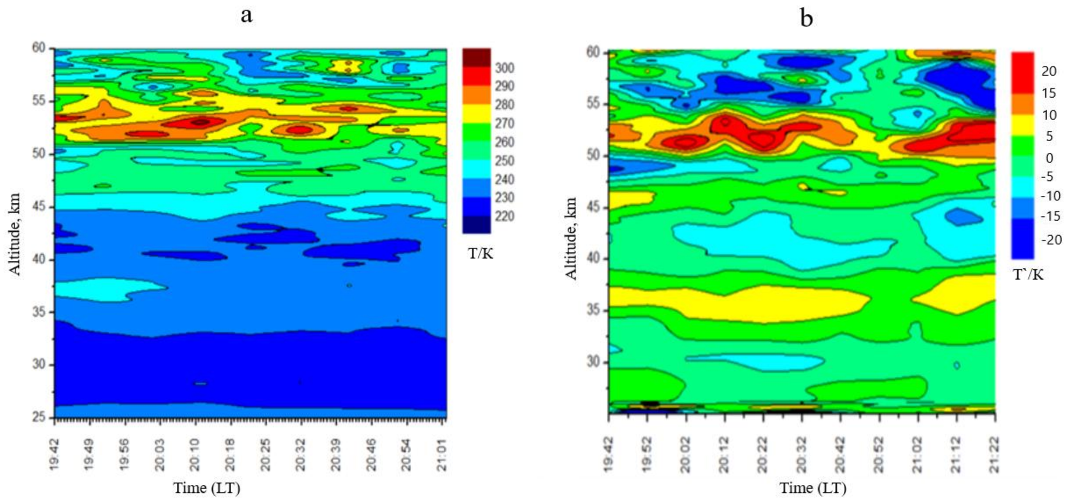


*Figure 1.* Dynamics of the atmospheric temperature profile (*a*) and temperature disturbances (*b*) on November 08, 2014 according to lidar measurements near Yakutsk. To improve perception, the interpolation was performed using the Kriging method in a special-purpose program

### 1.4. Calculation of GWPED per unit mass $E_{pm}$

A widely used physical quantity characterizing the IGW activity on the basis of atmospheric temperature profile variations is the GWPED. It is a good indicator of the gravity wave intensity. The GWPED per unit mass $E_{pm}$ is a measure of wave amplitude, whereas its vertical profile per unit volume $E_{pv}$ can be utilized as an indicator of wave dissipation. In this paper, we examine the GWPED per unit mass [Wilson et al., 1991]

$$E_{pm}(h) = \frac{1}{2}\frac{g^2}{N(h)^2}\left(\frac{T'(h)}{T_o(h)}\right)^2, \quad (2)$$

where $g$=9.7 m/s$^2$ is free fall acceleration; $T'(h)$ is the temperature variation; $T_o(h)$ is the background temperature; $N$ is the Brunt — Väisälä frequency

$$N(h)^2 = \frac{g}{T_o}\left(\frac{dT_o(h)}{dh} + \frac{g}{C_p}\right), \quad (3)$$

where $\frac{dT_o(h)}{dh}$ is the background temperature gradient; $C_p$=1004 J/(kg·K) is the specific heat of dry air at constant pressure. IGW-driven temperature variations generally increase with height due to a decrease in atmospheric density. This leads to a rise in $E_{pm}$ with height during undisturbed IGW propagation at constant winds. The GWPED per unit mass will increase as $\exp(h/H_{pm})$, where $H_{pm}$ is the height scale of atmospheric density:

$$E_{pm}(h) = E_{pm}(h_0)\exp\left(\frac{h-h_0}{H_{pm}}\right). \quad (4)$$

According to this definition, the height scale of density is an indicator of gravity wave energy dissipation, i.e., if $H_{pm}$>0 and $H_{pm}$>$H$ (the standard height scale for the middle atmosphere $H$=7 km), $E_{pm}$ increases with height more slowly than during conservative IGW propagation, and in this case IGWs are thought to dissipate [Mzé et al., 2014; Zhao et al., 2022a, b].

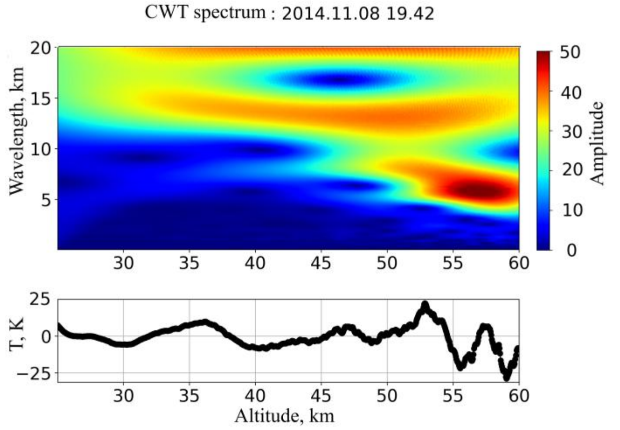


*Figure 2.* Wavelet transform of temperature variations

## 2. RESULTS AND DISCUSSION

Vertical profiles of monthly average $E_{pm}$ calculated for six winters from lidar observations over Yakutsk are presented in Figure 3. $E_{pm}$ averaged over six winters (black line) is seen to gradually increase from 11 J/kg at an altitude of 30 km to ~150 J/kg at an altitude of 55 km. Note that the IGW activity is maximum in winter and minimum in summer, with dominant wave periods from 6 to 8 hrs and vertical wavelengths from 4 to 18 km. The waves are saturated at an altitude of ~60 km [Rauthe et al., 2006; Khaykin et al., 2015]. The values we have obtained proved to be higher than those presented in other works [Wilson et al., 1991; Sivakumar et al., 2006; Kafle, 2009; Hei et al., 2008; Mzé et al., 2014; Ehard et al., 2014; Zhao et al., 2022a, b]. Notice that most of these studies use lidar measurement data from mid-latitude Eurasia. In high-latitude Europe, measurements have been made only a few times, and it must be considered that the climatic and geographic conditions there differ significantly from those in high-latitude Northeast Asia, where our measurements were carried out. At the same time, the IGW potential energy is higher at high latitudes, as has been found from both lidar and satellite measurements [Alexander et al., 2008]. Moreover, the scientific community has not fully standardized methods of calculating IGW characteristics in the atmosphere from lidar measurements. The difference between the methods of obtaining gravity wave parameters can also lead to the observed discrepancy in the results.

Note that in winters with major SSW events average $E_{pm}$ for the winter months is higher than those averaged over the entire observation period. Information on the SSW events recorded during this period is given in Table 3. The difference in $E_{pm}$ during the winter months of the same year reflects the nature of the destruction or displacement of the polar vortex. So, during the SSW event with a displaced polar vortex, the difference in $E_{pm}$ in December, January, and February of 2010–2011, 2015–2016 at altitudes from 40 to 50 km was up to 30 J /kg, whereas during the SSW event with a destructed polar vortex in 2011–2012 and 2012–2013 the spread of $E_{pm}$ values during these months was much wider, which was caused by a decrease in $E_{pm}$ in February. However, the interannual variability in the gravity wave activity reveals a positive correlation with the occurrence of stratospheric warmings. In years with major SSW, $E_{pm}$ was lower than in years without them.

The profiles in the winter period of 2014–2015, when a steady descending critical layer was detected at the stratopause (~50 km) during the three winter months, stand out among some vertical profiles of $E_{pm}$ (see Figure 3). Formation of this layer is likely to be induced by the minor SSW event in January 2015, which had a strong effect on the circulation and chemical processes in the stratosphere during the subsequent winter [Manney et al., 2015]. In Figure 3, we can also see regions where $E_{pm}$ changes very little or remains unchanged during the three winter months of interest.

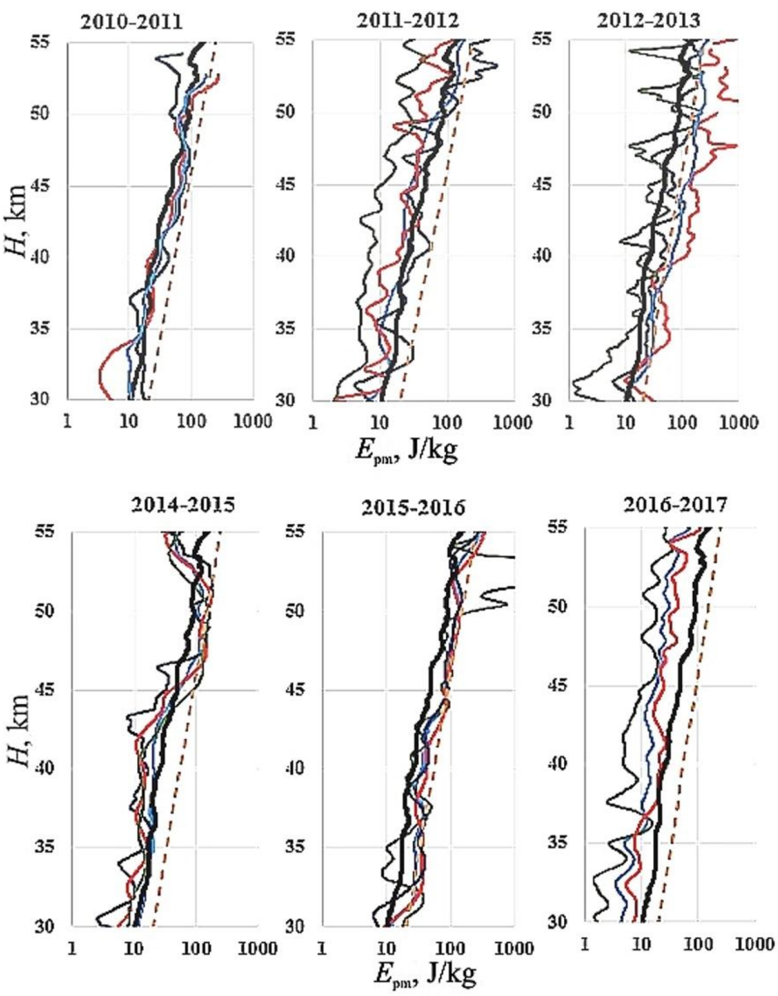


*Figure 3.* Vertical profiles of the IGW potential energy per unit mass $E_{pm}$ in winter months from 2010 to 2017 (logarithmic scale): blue — December, red — January, green — February, blue — seasonal average, black — averaged over 2010–2017; dashed brown line — height scale of atmospheric density (scale of conservative growth $H$=10)

Table 3

List of SSW events

| Year | Type | Class | Central date of SSW |
|---|---|---|---|
| 2011 | D | minor | Feb. 02, 2011 |
| 2012 | D | minor | Jan. 21, 2012 |
| 2013 | S | major | Jan. 06, 2013 |
| 2015 | D | minor | Jan. 05, 2015 |
| | F | minor | Mar. 26, 2015 |
| 2016 | D | minor | Feb. 09, 2016 |
| | F | major | Mar. 06, 2016 |
| 2017 | D | major | Feb. 01, 2017 |
| | F | minor | Feb. 27, 2017 |

These regions are located at an altitude of ~45 km and are particularly visible during the winter periods of 2014–2015 and 2015–2016. The same regions can be observed in [Ehard et al., 2014; Chu et al., 2018], but altitudes of the regions vary and most likely depend on the dynamic properties of the atmosphere at the observation point.

Further research is needed to study the gravity wave activity and its relationship with winds in order to explain the observed variability, as well as to better understand the activity of gravity waves associated with SSW.

## CONCLUSIONS

Analysis of lidar observations near Yakutsk during the winter periods from December 2010 to February 2017 shows the presence of QMWS at almost all nights. QMWS are mainly characterized by a downward phase progression corresponding to upward energy propagation. The main vertical lengths of IGWs and their $E_{pm}$ were calculated from temperature profile variations. We have obtained the following results:

- Vertical IGW lengths range from 2 to 15 km, with the most common wavelengths being 4–6 and 8–12 km. The prevailing vertical wavelengths presented in this paper do not contradict the results of other authors.
- The IGW potential energy per unit mass $E_{pm}$, averaged over all six winters (2010–2017), gradually increases from ~11 J/kg at an altitude of 30 km to ~150 J/kg at an altitude of 55 km.
- We have established that seasonal average $E_{pm}$, calculated from December to February, rises during major SSW events. During polar vortex splitting, the variability in the monthly average $E_{pm}$ profiles increases compared to their variability during the displacement of the vortex.

- We have found that in the height range of ~45 km $E_{pm}$ changes very little or remains unchanged during the three winter months we have examined, this is especially noticeable in the winter periods of 2014–2015 and 2015–2016.

The work was financially supported by the Russian Science Foundation (Grant No. 25-27-20119) https://rscf.ru/project/25-27-20119/. Experimental data was obtained within the framework of Government Assignment No. 125102712109-5.

## REFERENCES

Alexander M.J., Gille J., Cavanaugh C., et al. Global estimates of gravity wave momentum flux from High Resolution Dynamics Limb Sounder observations. *J. Geophys. Res.* 2008, vol. 113, iss. D15S18. https://doi.org/10.1029/2007JD008807.

Alpers M., Eixmann R., Fricke-Begemann C., et al. Temperature lidar measurements from 1 to 105 km altitude using resonance, Rayleigh, and rotational Raman scattering. *Atmos. Chem. Phys.* 2004, vol. 4, pp. 793–800. https://doi.org/10.5194/acpd-4-923-2004.

Cai X., Yuan T., Liu H.L. Large scale gravity waves perturbations in mesosphere region above Northern Hemisphere mid-latitude during autumn equinox: A joint study by Na Lidar and Whole Atmosphere Community Climate Model. *Ann. Geophys.* 2017, vol. 35, pp. 181–188. https://doi.org/10.5194/angeo-35-181-2017.

Chanin M.L., Hauchecorne A. Lidar observation of gravity and tidal waves in the stratosphere and mesosphere. *J. Geophys. Res.* 1981, vol. 86, pp. 9715–9721. https://doi.org/10.1029/JC086iC10p09715.

Chu X., Zhao J., Lu X., et al. Lidar observations of stratospheric gravity waves from 2011 to 2015 at McMurdo (77.84° S, 166.69° E), Antarctica: 2. Potential energy densities, lognormal distributions, and seasonal variations. *J. Geophys. Res.: Atmos.* 2018, vol. 123, pp. 7910–7934. https://doi.org/10.1029/2017JD02786.

Dornbrack A., Gisinger S., Kaifler B. On the interpretation of gravity wave measurements by ground-based lidars. *Atmosphere*. 2017, vol. 8, iss. 3, p 49. https://doi.org/10.3390/atmos8030049.

Ehard B., Achtert P., Gumbel J. Long-term lidar observations of wintertime gravity wave activity over northern Sweden. *Ann. Geophys*. 2014, vol 32, pp 1395–1405. https://doi.org/10.5194/angeo-32-1395-2014.

Fritts D.C., Alexander M.J. Gravity wave dynamics and effects in the middle atmosphere. *Rev. Geophys*. 2003, vol. 41, iss. 1003. https://doi.org/10.1029/2001RG000106.

Gisinger S., Polichtchouk I., Dornbrack A.D., et al. Gravity-wave-driven seasonal variability of temperature differences between ECMWF IFS and Rayleigh lidar measurements in the lee of the Southern Andes. *J. Geophys. Res.: Atmos.* 2022, vol. 127. https://doi.org/10.1029/2021JD036270.

Hei H., Tsuda T., Hirooka T. Characteristics of atmospheric gravity wave activity in the polar regions revealed by GPS radio occultation data with CHAMP. *J. Geophys. Res*. 2008, vol. 113, D04107. https://doi.org/10.1029/2007JD008938.

Holton J.R. The role of gravity wave induced drag and diffusion in the momentum budget of the mesosphere. *J. Atmos. Sci*. 1982, vol. 39, iss. 4, pp. 791–799.

Kafle Durga N. *Rayleigh-Lidar Observations of Mesospheric Gravity Wave Activity above Logan, Utah. A dissertation submitted in partial fulfillment of the requirements for the degree Doctor of Philosophy in Physics.* Utah State University, 2009, 209 p. https://doi.org/10.26076/0d8f-a7f4.

Kaifler N., Kaifler B., Ehard B., et al. Observational indications of downward propagating gravity waves in middle atmosphere lidar data. *J. Atmos. Solar-Terr. Phys.* 2017, vol. 162, pp. 16–27. https://doi.org/10.1016/j.jastp.2017.03.003.

Kaifler N., Kaifler B., Dornbrack A., et al. Lidar observations of large-amplitude mountain waves in the stratosphere above Tierra del Fuego, Argentina. *Sci. Rep.* 2020, 14529. https://doi.org/10.1038/s41598-020-71443-7.

Khaykin S.M., Hauchecorne A., Mzé N., Keckhut P. Seasonal variation of gravity wave activity at mid-latitudes from 7 years of COSMIC GPS and Rayleigh lidar temperature observations. *Geophys. Res. Lett.* 2015, vol. 42, iss. 4, pp. 1251–1258. https://doi.org/10.1002/2014GL062891.

Lindzen R.S. Turbulence and stress owing to gravity wave and tidal breakdown. *J. Geophys. Res.* 1981, vol. 86, iss. C10, pp. 9707–9714. https://doi.org/10.1029/JC086iC10p09707.

Manney G.L., Lawrence Z.D., Santee M.L., et al. A minor sudden stratospheric warming with a major impact: Transport and polar processing in the 2014/2015 Arctic winter. *Geophys. Res. Lett.* 2015, vol. 42, iss. 18, pp. 7808–7816. https://doi.org/10.1002/2015GL065864.

Matsuno T. A quasi one-dimensional model of the middle atmosphere circulation interacting with internal gravity waves. *J. Meteorol. Soc. Japan.* 1982, vol. 60, iss. 1, pp. 215–226. https://doi.org/10.2151/jmsj1965.60.1_215.

Mzé N., Hauchecorne A., Keckhut P., Thétis M. Vertical distribution of gravity wave potential energy from long-term Rayleigh lidar data at a northern middle latitude site. *J. Geophys. Res.: Atmos.* 2014, vol. 119, iss. 21, pp. 12069–12083. https://doi.org/10.1002/2014JD022035.

Rauthe M., Gerding M., Höffner J., Lübken F.-J. Lidar temperature measurements of gravity waves over Kühlungsborn (54° N) from 1 to 105 km: A winter-summer comparison. *J. Geophys. Res.: Earth Surf.* 2006, vol. 111, D24108. https://doi.org/10.1029/2006JD007354.

Reichert R., Kaifler N., Kaifler B. Limitations in wavelet analysis of non-stationary atmospheric gravity wave signatures in temperature profiles. *Atmos. Meas. Tech.* 2024, vol. 17, iss. 15, pp. 4659–4673. https://doi.org/10.5194/amt-17-4659-2024.

Sivakumar V., Rao P.B., Bencherif H. Lidar observations of middle atmospheric gravity wave activity over a low–latitude site (Gadanki, 13.5° N, 79.2° E). *Ann. Geophys.* 2006, vol. 24, iss. 3, pp. 823–834. https://doi.org/10.5194/angeo-24-823-2006.

Strelnikova I., Baumgarten G., Lübken F.-J. Advanced hodograph-based analysis technique to derive gravity-wave parameters from lidar observations. *Atmos. Meas. Tech.* 2020, vol. 13, iss. 2, pp. 479–499. https://doi.org/10.5194/amt-13-479-2020.

Thurairajah B., Collins R.L., Harvey V.L., et al. Rayleigh lidar observations of reduced gravity wave activity during the formation of an elevated stratopause in 2004 at Chatanika, Alaska (65° N, 147° W). *J. Geophys. Res.: Earth Surf.* 2010, vol. 115, D13109. https://doi.org/10.1029/2009JD013036.

Titov S., Nikolashkin S. Mobile lidar station. *Proc. SPIE 11560. 26th International Symposium on Atmospheric and Ocean Optics, Atmospheric Physics*. Moscow, 2020, 1156091. https://doi.org/10.1117/12.2576118.

Torrence C., Compo G.P. A Practical Guide to Wavelet Analysis. *Bull. Am. Meteorol. Soc.* 1998, vol. 79, pp. 61–78. https://doi.org/10.1175/1520-0477(1998)079<0061:APGTWA>2.0.CO;2.

Whiteway J.A., Carswell A.I. Lidar observations of gravity wave activity in the upper stratosphere over Toronto. *J. Geophys. Res.: Earth Surf.* 1995, vol. 100, iss. D7, pp. 14113–14124. https://doi.org/10.1029/95JD00511.

Wilson R., Chanin M.L., Hauchecorne A. Gravity waves in the middle atmosphere observed by Rayleigh lidar: 2. Climatology. *J. Geophys. Res.: Earth Surf.* 1991, vol. 96, iss. D3, pp. 5169–5183. https://doi.org/10.1029/90JD02610.

Zhao H., Hu W.X., Yan Z., et al. Atmospheric gravity wave potential energy observed by Rayleigh lidar above Jiuquan (40° N, 95° E), China. *Atmosphere.* 2022a, vol. 13, iss. 7, 1098. https://doi.org/10.3390/atmos130711098.

Zhao W., Hu X., Pan W., et al. Mesospheric gravity wave potential energy density observed by Rayleigh lidar above Golmud (36.25° N, 94.54° E), Tibetan plateau. *Atmosphere.* 2022b, vol. 13, iss. 7, 1084. https://doi.org/10.3390/atmos13071084.

URL: https://rscf.ru/project/25-27-20119/ (accessed June 22, 2026).

Original Russian version: Titov S.V., Nikolashkin S.V., Sidorov N.E., published in Solnechno-zemnaya fizika. 2026, vol. 12, no. 3, pp. 107–113. https://doi.org/10.12737/szf-123202611. 

*How to cite this article*

Titov S.V., Nikolashkin S.V., Sidorov N.E. The potential energy density of gravity waves in the winter stratosphere and lower mesosphere from lidar measurements over Yakutsk. *Sol.-Terr. Phys*. 2026, vol. 12, iss. 3, pp. 95–101. https://doi.org/10.12737/stp-123202611.